Control of spin current by a magnetic YIG substrate in NiFe/Al nonlocal spin valves

Control of spin current by a magnetic YIG substrate in NiFe/Al nonlocal spin valves

F. K. Dejene,[1,*] N. Vlietstra,[1] D. Luc,[2] X. Waintal,[2] J. Ben Youssef,[3] and B. J. van Wees[1]

[1] *Physics of Nanodevices, Zernike Institute for Advanced Materials, University of Groningen, 9747AG, Groningen, The Netherlands*
[2] *CEA-INAC/UJF Grenoble 1, SPSMS UMR-E 9001, Grenoble F-38054, France*
[3] *Universit de Bretagne Occidentale, Laboratoire de Magnetisme de Bretagne CNRS, 6 Avenue Le Gorgeu, 29285 Brest, France*

(Dated: September 30, 2018)

We study the effect of a magnetic insulator (Yttrium Iron Garnet - YIG) substrate on the spin transport properties of $Ni_{80}Fe_{20}$/Al nonlocal spin valve (NLSV) devices. The NLSV signal on the YIG substrate is about 2 to 3 times lower than that on a non magnetic SiO_2 substrate, indicating that a significant fraction of the spin-current is absorbed at the Al/YIG interface. By measuring the NLSV signal for varying injector-to-detector distance and using a three dimensional spin-transport model that takes spin current absorption at the Al/YIG interface into account we obtain an effective spin-mixing conductance $G_{\uparrow\downarrow} \simeq 5-8\times10^{13}\ \Omega^{-1}\mathrm{m}^{-2}$. We also observe a small but clear modulation of the NLSV signal when rotating the YIG magnetization direction with respect to the fixed spin polarization of the spin accumulation in the Al. Spin relaxation due to thermal magnons or roughness of the YIG surface may be responsible for the observed small modulation of the NLSV signal.

The coupled transport of spin, charge and heat in nonmagnetic (N) metals deposited on the magnetic insulator $Y_3Fe_5O_{12}$ (YIG) has led to new spin caloritronic device concepts such as thermally driven spin currents, the generation of spin angular momentum via the spin Seebeck effect (SSE) [1], spin pumping from YIG to metals [2], spin-orbit coupling (SOC) induced magnetoresistance effects [3, 4] and the spin Peltier effect, i.e., the inverse of the SSE that describes cooling/heating by spin currents [5]. In these spin caloritronic phenomena, the spin-mixing conductance $G_{\uparrow\downarrow}$ of the N/YIG interface controls the transfer of spins from the conduction electrons in N to the magnetic excitations (magnons) in the YIG, or *vice versa* [6–10]. The interconversion of spin current to a voltage employs the (inverse) spin Hall effect in heavy-metals such as Pt or Pd. The possible presence of proximity induced magnetism in these metals is reported to introduce spurious magnetothermoelectric effects [11, 12] or enhance $G_{\uparrow\downarrow}$ [7]. Owing to the short spin-diffusion length λ in these large SOC metals, the applicability of the diffusive spin-transport model is also questionable. Experimental measurements that alleviate these concerns are however scarce and hence are highly required.

In this article, we investigate the interaction of spin current (in the absence of a charge current) with the YIG magnetization using the NLSV geometry [13–15]. Using a metal with low SOC and long spin-diffusion length allows to treat our experiment using the diffusive spin-transport model. We find that the NLSV signal on the YIG substrate is two to three times lower than that on the SiO_2 substrate, indicating significant spin-current absorption at the Al/YIG interface. By varying the angle between the induced spin accumulation and the YIG magnetization direction we observe a small but clear modulation of the NLSV signal. We also find that modifying the quality of the Al/YIG interface, using different thin-film deposition methods [4], influences $G_{\uparrow\downarrow}$ and hence the size of the spin current flowing at the Al/YIG interface. Recently, a low-temperature measurements of a similar effect was reported by Villamor *et al.*[16] in Co/Cu devices where $G_{\uparrow\downarrow} \sim 10^{11}\Omega^{-1}\mathrm{m}^{-2}$ was estimated, two orders of magnitude lower than in the literature [4, 8]. Here, we present a room-temperature spin-transport study in transparent $Ni_{80}Fe_{20}$ (Py)/Al NLSV devices.

Figure 1 depicts the concept of our experiment. A non-magnetic metal (green) deposited on the YIG connects the two in-plane polarized ferromagnetic metals F_1 and F_2, which are used for injecting and detecting spin currents, respectively. A charge current through the F_1/Al interface induces a spin accumulation $\boldsymbol{\mu}_s(\vec{r}) = (0, \mu_s, 0)^T$ that is polarized along the $\hat{y}$ direction, parallel to the magnetization direction of F_1. This non-equilibrium $\boldsymbol{\mu}_s$, the difference between the electrochemical potentials for spin up and spin down electrons, diffuses to both $+\hat{x}$ and $-\hat{x}$ directions of F_1/Al interface with an exponential decay characterized by the spin diffusion length λ_N. Spins arriving at the detecting F_2/Al interface give rise to a nonlocal voltage V_{nl} that is a function of the relative magnetic configuration of F_1 and F_2, being minimum (maximum) when F_1 and F_2 are parallel (antiparallel) to each other.

For NLSV devices on a SiO_2 substrate, spin relaxation proceeds via electron scattering with phonons, impurities or defects present in the spin transport channel, also known as the Elliot-Yafet (EY) mechanism. The situation is different for a NLSV on the magnetic YIG substrate where additional spin relaxation due to thermal magnons in the YIG and/or interfacial spin orbit coupling can be mediated by direct spin-flip scattering or spin-precession. Depending on the magnetization direction $\hat{m}$ of the YIG with respect to $\boldsymbol{\mu}_s$ spins incident at

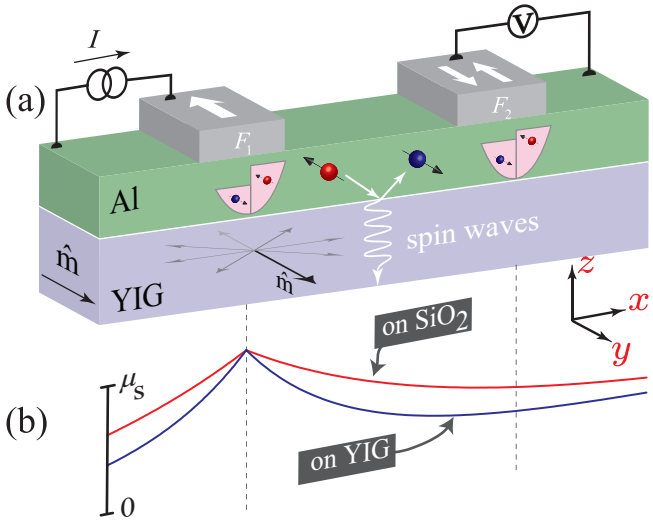

FIG. 1. (Color online) Concept of the experiment for $\hat{m} \parallel \boldsymbol{\mu_s}$. (a) A charge current through the F_1/Al interface creates a spin accumulation $\boldsymbol{\mu}_s$ in the Al. The diffusion of $\boldsymbol{\mu}_s$ to the F_2/Al interface is affected by spin-flip relaxation at the Al/YIG interface. Scattering of a spin up electron (s=$\hbar/2$) into spin down electron (s=$-\hbar/2$) is accompanied by magnon emission (s=$\hbar$) creating a spin current that is minimum (maximum) when $\hat{\mu}_s$ is parallel (perpendicular) to the magnetization of the YIG. (b) Profile of $\boldsymbol{\mu}_s$ along the Al strip on a SiO_2 (red) and YIG (blue) substrate. The spin accumulation at the F_2/Al is lower for the YIG substrate compared to that on SiO_2.

the Al/YIG surface are absorbed ($\hat{m} \perp \boldsymbol{\mu}_s$) or reflected ($\hat{m} \parallel \boldsymbol{\mu}_s$) thereby causing a spin current density $\boldsymbol{j}_s(\vec{r})$ through the Al/YIG interface [9]

$$\boldsymbol{j}_s(\hat{m})|_{z=0} = G_r \hat{m} \times (\hat{m} \times \boldsymbol{\mu}_s) + G_i(\hat{m} \times \boldsymbol{\mu}_s) + G_s \boldsymbol{\mu}_s. \quad (1)$$

Here $\hat{m} = (m_x, m_y, 0)^T$ is a unit vector parallel to the in-plane magnetization of the YIG, G_r (G_i) is the real (imaginary) part of the spin-mixing conductance per unit area and G_s is a spin-sink conductance that can be interpreted as an effective spin-mixing conductance that quantifies spin-absorption (flip) effects that is independent of the angle between $\hat{m}$ and $\boldsymbol{\mu}_s$.

When $\hat{m} \parallel \boldsymbol{\mu}_s$ some of the spins incident on the YIG are reflected back into the Al while some fraction is absorbed by the YIG. The absorption of the spin-current in this collinear case is governed by a spin-sinking effect either due to (i) the thermal excitation of the YIG magnetization (thermal magnons) or (ii) spin-flip processes due to interface spin orbit effects or magnetic impurities present at the interface. This process can be characterized by an effective spin-mixing interface conductance G_s which, at room temperature, is about 20% of G_r [5]. Because of this additional spin-flip scattering, the maximum NLSV signal on the YIG substrate should also be smaller than that on the SiO_2. When $\hat{m} \perp \boldsymbol{\mu}_s$ spins arriving at the Al/YIG interface are absorbed. In this case all three terms in Eq. (1) contribute to a maximum flow of spin current through the interface. The nonlocal voltage measured at F_2 is hence a function of the angle between $\hat{m}$ and $\boldsymbol{\mu}_s$ and should reflect the symmetry of Eq. 1.

Fig. 2(a) shows the scanning electron microscope image of the studied NLSV device that was prepared on a 200-nm thick single-crystal YIG, having very low coercive field [2, 4, 17], grown by liquid phase epitaxy on a 500 μm thick (111) $Gd_3Ga_5O_{12}$ (GGG) substrate. It consists of two 20-nm thick $Ni_{80}Fe_{20}$ (Py) wires connected by a 130-nm thick Al cross. A 5 nm-thick Ti buffer layer was inserted underneath the Py to suppress direct exchange coupling between the Py and YIG. We studied two types of devices, hereafter named Type-A and Type-B devices. In Type-A devices (4 devices), prior to the deposition of the Al (by electron beam evaporation), Ar ion milling of the Py surface was performed to ensure a transparent Py/Al interface. This process, however, introduces unavoidable milling of the YIG surface thereby introducing disordered Al/YIG interface with lower $G_{\uparrow\downarrow}$ [18]. To circumvent this problem, in Type-B devices (2 devices), we first deposit a 20 nm-thick Al strip (by DC sputtering) between the injector and detector Py wires. Sputtering is reported to yield a better interface [4]. Next, after Ar ion milling of the Py and sputtered-Al surfaces, a 130 nm-thick Al layer was deposited using e-beam evaporation. Similar devices prepared on SiO_2 substrate were also investigated. All measurements were performed at room temperature using standard low frequency lock-in measurements.

The NLSV resistance $R_{\rm nl} = V_{\rm nl}/I$ as a function of the applied in-plane magnetic field (along $\hat{y}$) is shown in Fig. 2(b), both for SiO_2 (red and orange) and YIG (blue) samples. Note that the magnetizations of the injector, detector and YIG are all collinear and hence no initial transverse spin component is present. The spin valve signal, defined as the difference between the parallel R_P and anti-parallel R_{AP} resistance values, $R_{SV} = R_P - R_{AP}$ on the YIG substrate is about two to three times smaller than that on the SiO_2 substrate. This reduction in the NLSV signal indicates the presence of an additional spin-relaxation process even for $\hat{m} \parallel \boldsymbol{\mu}_s$. Assuming an identical spin injection efficiency in both devices, this means that spin relaxation in the Al on the YIG substrate occurs on an effectively shorter spin relaxation length λ_N. To properly extract λ_N we performed several measurements for varying distance between the Py wires, as shown in Figure 2(c) both on SiO_2 (red diamond) and YIG (blue square) substrates. Also shown are dashed-line fits using the expression for the nonlocal spin valve signal R_{SV} obtained from a one-dimensional spin transport theory given by [14]

$$R_{SV} = \frac{\alpha_F^2 R_N e^{-d/2\lambda_N}}{(\frac{R_F}{R_N}+1)[\frac{R_F}{R_N}\sinh(d/2\lambda_N) + \cosh(d/2\lambda_N)]}. \quad (2)$$

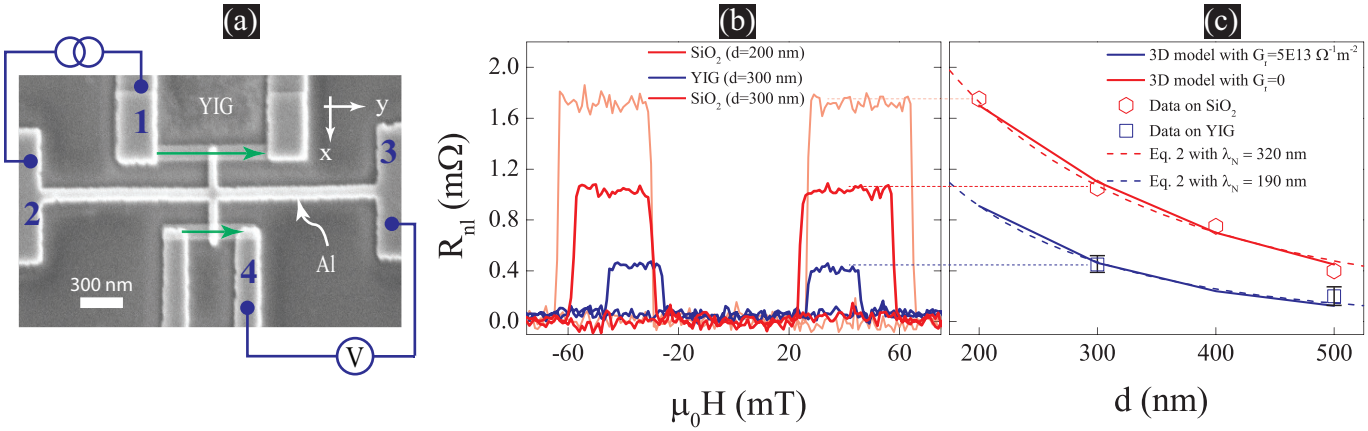

FIG. 2. (Color online) (a) Scanning electron microscopy image of the measured Type-A device. Two Py wires (indicated by green arrows) are connected by an Al cross. A charge current I from contact 1 to 2 creates a spin accumulation at the F_1/Al interface that is detected as a nonlocal spin voltage $V_{\rm nl}$ using contacts 3 and 4. (b) The NLSV resistance $R_{\rm nl} = V_{\rm nl}/I$ for representative YIG (blue) and SiO_2 (red and orange) NLSV samples. For comparison, a constant background resistance has been subtracted from each measurement. (c) Dependence of the NLSV signal on the spacing d between the injecting and detecting ferromagnetic wires together with calculated spin signal values using a 1D (dashed lines) and 3D (solid lines) spin-transport model. For each distance d between the injector and detector several devices were measured, with the error bars indicating the spread in the measured signal.

Here $R_F = (1-\alpha_F^2)\frac{\lambda_F}{\sigma_F}$ and $R_N = \frac{\lambda_N}{\sigma_N}$ are spin area resistance of the ferromagnetic (F) and non-magnetic (N) metals, respectively. λ_N and λ_F are the corresponding spin diffusion lengths, σ_F (σ_N) is the electrical conductivity of the F (N), α_F is the spin polarization of F and d is the distance between the injecting and detecting ferromagnetic electrodes. Fitting the SiO_2 data using Eq. (2), we extract α_F =0.32 and λ_{N,SiO_2} =320 nm, which are both in good agreement with reported values [13–15]. A similar fitting procedure for the YIG data, assuming an identical spin injection efficiency, yields an effectively shorter spin-diffusion length $\lambda_{N,\rm YIG}$=190 nm due to the additional spin-flip scattering at the Al/YIG interface. This value of $\lambda_{N,\rm YIG}$ therefore contains important information regarding an effective spin-mixing conductance G_s that can be attributed to the interaction of spins with thermal magnons in the YIG. When spin precession, due to the applied external field as well as the effective field due to G_i is disregarded, we can now estimate G_s by relating $\lambda_{N,\rm YIG}$ to λ_{N,SiO_2} via G_s as (see Supplemental Material [19], Sec. I):

$$\frac{1}{\lambda_{N,\rm YIG}^2} = \frac{1}{\lambda_{N,SiO_2}^2} + \frac{1}{\lambda_r^2}, \tag{3}$$

with $\lambda_r^{-2} = 2G_s/t_{Al}\sigma_N$ [19]. Using the extracted values from the fit, σ_N=2×10^7 S/m and t_{Al}=130 nm, we extract $G_s \simeq 2.5\times10^{13}\ \Omega^{-1}\ {\rm m}^{-2}$, which is about 25% of the maximum $G_r \sim 10^{14}\Omega^{-1}{\rm m}^{-2}$ reported for Pt/YIG [4, 7] and Au/YIG [8] interfaces.

To quantify our results we performed three-dimensional finite element simulations using COMSOL Multiphysics (3D-FEM) [19, 20] that uses a set of equations that are equivalent to the continuous random matrix theory in 3 dimensions (CRMT3D) [21]. The charge current $j_c^\alpha(\vec{r})$ and spin current $\boldsymbol{j}_s^\alpha(\vec{r})$, (where $\alpha \in x,y,z$), are linked to their corresponding driving forces via the electrical conductivity as

$$\begin{pmatrix} j_c^\alpha(\vec{r}) \\ \boldsymbol{j}_s^\alpha(\vec{r}) \end{pmatrix} = -\begin{pmatrix} \sigma & \alpha_F\sigma \\ \alpha_F\sigma & \sigma \end{pmatrix}\begin{pmatrix} \vec{\nabla}\mu_c \\ \vec{\nabla}\boldsymbol{\mu}_s \end{pmatrix} \tag{4}$$

where $\mu_c = (\mu_\uparrow + \mu_\downarrow)/2$ and $\boldsymbol{\mu}_s = (\mu_\uparrow - \mu_\downarrow)/2$ are the charge and spin accumulation chemical potentials, respectively. We supplement Eq. (4) by the conservation laws for charge ($\nabla\cdot j_c^\alpha(\vec{r}) = 0$) and spin current ($\nabla\cdot\boldsymbol{j}_s = (1-\alpha_F^2)\sigma\left[\boldsymbol{\mu}_s/\lambda^2 + \vec{\omega}_L\times\boldsymbol{\mu}_s\right]$) where $\vec{\omega}_L = g\mu_B\vec{B}/\hbar$ with $g = 2$ is the Larmor precession frequency due to spin precession in an in-plane magnetic field $\vec{B} = (B_x, B_y, 0)^T$ and μ_B is the Bohr magneton (see Supplemental Material [19], Sec. II). To include spin-mixing at the Al/YIG interface we impose continuity of the spin current $\boldsymbol{j}_s$ at the interface using Eq. (1). The input material parameters such as σ, λ and α_F are taken from Refs. 22 and 23.

The calculated spin signals obtained from our 3D-FEM are shown in Fig. 2(c) for samples on SiO_2 (red solid line) and YIG (blue solid line) substrates. By matching the experimentally measured NLSV signal on the SiO_2 substrate with the calculated values in the model we obtain $\alpha_F = 0.3$ and λ_N =350 nm. Using these two values and setting $G_s \simeq 5\times10^{13}\ \Omega^{-1}{\rm m}^{-2}$ well reproduces the measured spin signal on the YIG substrate. This value of G_s obtained here is consistent with that extracted from our 1D analysis based on Eq. 2. Hence, the interaction of spins with the YIG magnetization, as modeled here, can

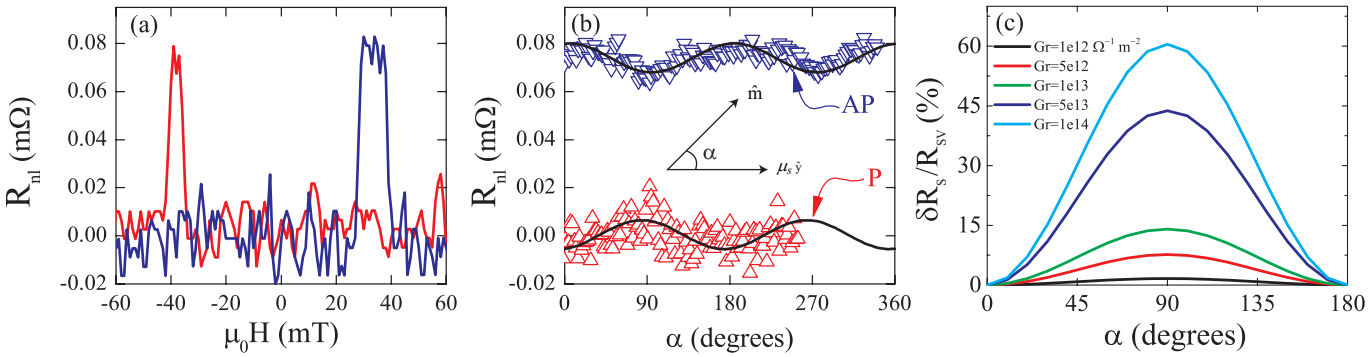

FIG. 3. (Color online) (a) Nonlocal spin valve resistance R_{nl} of a Type-B device with d=500 nm between injecting and detecting Py wires and t_{Al}=130 nm. A constant background resistance of 117 mΩ was subtracted from the original data. (b) Angular dependence of the NLSV signal in the parallel and antiparallel configurations. The AP curve is average of 10 measurements and that of the P state is a single scan. Both resistance states exhibit a cos(2α) dependence on the angle between $\hat{m}$ and $\boldsymbol{\mu}_s$. The black solid lines are calculated using the 3D-FEM model for $G_r = 1 \times 10^{13}\Omega^{-1}\mathrm{m}^{-2}$ that show a percentage modulation of only 12% corresponding to the green curve in (c) $\delta R_{SV}/R_{SV}$ is plotted. The angular dependent measurement in (b) is from a device for which complete set of measruements were peformed. A spin valves measurement as in (a) was also performed for another device with $d = 300$ nm.

capture the concept of spin-mixing conductance being responsible for the observed reduction in the spin signal.

In the following we investigate the dependence of R_{nl} on the angle α between $\boldsymbol{\mu}_s$ and $\hat{m}$. We rotate the sample under the application of a very low in-plane magnetic field B $\leq$5 mT, enough to saturate the low-coercive ($\leq$ 0.5 mT) YIG magnetization [4, 5] but smaller than the coercive fields of F_1 and F_2 (~20 mT). This condition is important to maintain fixed polarization axes of $\boldsymbol{\mu}_s$, along the magnetization direction of the injecting ferromagnet, and also have a well defined α. The result of such measurement in a Type-B device is shown in Fig. 3(b) for d = 400 nm between F_1 and F_2. Although the measured NLSV signal [Fig.3(a)] is smaller than in Type-A devices, possibly due to a better Al/YIG interface, R_{nl} exhibits a cos(2α) behavior with a maximum (minimum) for $\alpha = 0$ ($\alpha = \pi/2$), consistent with Eq. (1). However, the maximum change (modulation) of the signal δR_s=$R_{nl}(\alpha = 0) - R_{nl}(\alpha = \pi/2)$) is only 12% of the total spin signal R_{SV}, which is at odds with the large spin-mixing conductance estimated from Fig. 2(b). From anistropic magnetoresistance measurements we exclude the possibility of any rotation of the magnetization of the injector and detector as the cause for the observed modulation in the NLSV signal (see Supplemental Material [19], Sec. III-B).

Using the 3D-FEM we calculated the angular dependence of R_{SV} for various values of G_r where the percentage modulation $\delta R_s/R_{SV}$ is plotted as a function of α, as shown in Fig. 3(c). The G_r value of 1×10^{13} $\Omega^{-1}\mathrm{m}^{-2}$ extracted from the NLSV signal modulation experiment is one order of magnitude less than reported elsewhere [4]. This can be possibly caused by the presence of disordered Al/YIG interface with r.m.s. roughness of 0.8 nm (as measured by AFM), which is close to the magnetic coherence volume $\sqrt[3]{V_c} \simeq 1.3$ nm [6] of the YIG. This length scale determines the effective width of the Al/YIG interface and also the extent to which spin current from the Al is felt by the YIG magnetization [6, 24]. Furthermore, the fact that there exists a finite spin-mixing when $\alpha = 0$, as discussed above, can also explain the observed small modulation. It is important to note that in our experiments the non-equilibrium spin accumulation induced by electrical spin injection into Al has a spin-polarization strictly along the direction of the magnetization of F_1, which lies along the $\hat{y}$ axis. In the measurement results shown in Figs. 1(b) and 2(b) the magnetization of the F_2 is always kept either parallel or antiparallel to the detector F_1. This ensures that it is only the $\hat{y}$ component of the spin accumulation that is measured in our experiments as it is insensitive to other two spin-polarization

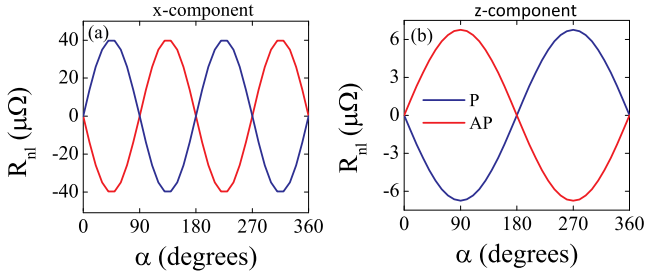

FIG. 4. (Color online) Calculated NLSV signals showing the (a) x-component and (b) z-component of the NLSV signal R_{nl} in the parallel (red) and antiparallel (blue) magnetization configurations of the injector and detector ferromagnetic contacts for $G_r = 1 \times 10^{13}$ $\Omega^{-1}\mathrm{m}^{-2}$ and $G_i = 0.1G_r$. Even if the injected spin accumulation is polarized along the magnetization direction of the injecting electrode F_1, its interaction with the magnons via the spin-mixing conductance induces these spin accumulation components.

directions. It is however possible that the interaction of the initially injected spin accumulation with the YIG magnetization, via $G_{\uparrow\downarrow}$, to induce a finite NLSV signal with components polarized along the $\hat{x}$- and $\hat{z}$-directions.

Figure 4 shows the angular dependence of the $\hat{x}-$ and $\hat{z}-$ component of the NLSV signal as calculated using our 3D-FEM. While the $\hat{z}$ component exhibits a $\sin(\alpha)$ dependence, the $\hat{x}$ component shows a $\sin(2\alpha)$ dependence which is consistent with Eq. (1). The size of the modulation is determined by G_r for the $\hat{x}-$ component and by G_i for the $\hat{z}-$ component. In a collinear measurement configuration these transverse spin accumulation components can induce local magnetization dynamics by exerting a spin transfer torque to the YIG. Separately measuring these spin accumulation using ferromagnetic contacts magnetized along the $\hat{x}$ and $\hat{z}$ directions can be an alternative way to extract $G_{\uparrow\downarrow}$.

In summary, we studied spin injection and relaxation at the Al/YIG interface in $Ni_{80}Fe_{20}$/Al lateral spin valves fabricated on YIG. The samples on the YIG substrate yield NLSV signals that are two to three times lower than those grown on standard SiO_2 substrates, indicating spin-current absorption by the magnetic YIG substrate. We also observed a small but clear modulation of the measured NLSV signal as a function of the angle between the spin accumulation and magnetization of the YIG. The presence of a disordered Al/YIG interface combined with a spin-flip (sink) process due to thermal magnons or interface spin-orbit effects can be accounted for this small modulation. Using finite element magnetoelectronic circuit theory as well as additional control experiments, we establish the concept of collinear (effective) spin mixing conductance due to the thermal magnons in the YIG. Our result therefore calls for the inclusion of this term in the analysis of spintronic and spin caloritronic phenomena observed in metal/YIG bilayer systems.

The authors thank M. de Roosz and J.G. Holstein for technical assistance. This work is part of the research program of the Foundation for Fundamental Research on Matter (FOM) and is supported by NanoLab NL, EU-FET Grant InSpin 612759 and the Zernike Institute for Advanced Materials.

SUPPLEMENTAL MATERIAL

I. Derivation for the effective spin relaxation length in the collinear case

The spin accumulation $\boldsymbol{\mu}_s$, with polarization parallel to the magnetization direction of F_1 (see Fig. S5), injected in the Al is governed by the Valet-Fert spin diffusion equation [25] $\left[\partial_x^2+\partial_y^2+\partial_z^2\right]\boldsymbol{\mu}_s = \boldsymbol{\mu}_s/\lambda_N^2$, which can be re-arranged to give

$$\partial_x^2\boldsymbol{\mu}_s = \boldsymbol{\mu}_s/\lambda_N^2 - \partial_z^2\boldsymbol{\mu}_s. \tag{5}$$

Here we assume that, for a homogeneous system, the spin current along the $\hat{y}$-direction is zero. As discussed in the main text, when the YIG magnetization direction $\hat{m} \parallel \boldsymbol{\mu}_s$ the spin current $\boldsymbol{j}_s^{z=0}$ at the Al/YIG interface, in the $\hat{z}$-direction, is governed by the spin sink term G_s in Eq. 1 of the main text. Applying spin current continuity condition at the Al/YIG interface we find that

$$\frac{\sigma_N}{2}\partial_z\boldsymbol{\mu}_s = G_s\boldsymbol{\mu}_s \tag{6}$$

where σ_N is the conductivity of the normal metal. Now after re-arranging Eq. (6) to obtain $\partial_z\boldsymbol{\mu}_s$, differentiating it once and using $\partial_z\boldsymbol{\mu}_s = \boldsymbol{\mu}_s/t_{Al}$, where t_{Al} is the thickness of the Al, we obtain

$$\partial_z^2\boldsymbol{\mu}_s = -\frac{2G_s\boldsymbol{\mu}_s}{\sigma_N t_{Al}}. \tag{7}$$

Substituting Eq. (7) into Eq. (5) we obtain a modified VF-spin diffusion equation that contains two length scales

$$\partial_x^2\boldsymbol{\mu}_s = \boldsymbol{\mu}_s/\lambda_N^2 + 2G_r\boldsymbol{\mu}_s/\sigma_N t_{Al}, \tag{8a}$$

$$= \frac{\boldsymbol{\mu}_s}{\lambda_N^2} + \frac{\boldsymbol{\mu}_s}{\lambda_r^2}, \tag{8b}$$

where we defined a new length scale $\lambda_r^{-2} = 2G_s/\sigma_N t_{Al}$ that, together with the λ_N, re-defines an effective spin relaxation length $\lambda_{\text{eff}}^{-2} = \lambda_N^{-2} + \lambda_r^{-2}$. This effective spin relaxation length in the Al channel is weighted by the spin-mixing conductance G_s of the Al/YIG interface. The modulation of the NLSV signal observed in our measurements is hence determined by the interplay between these two length scales, λ_N and λ_r. While the first quantifies the effective spin-conductance of the Al channel ($G_N = \sigma_N A_N/\lambda_{Al}$) over the spin relaxation length, the second is a measure of the quality of the Al/YIG interface and is set by G_s. For the devices investigated in this work, using $A_N = t_{Al}w_{Al}$ with the width of the Al channel $w_{Al} = 100$nm and $\sigma_{Al} = 2\times10^7$S/m, we obtain $A_N^{-1}G_N \simeq 6\times10^{13}\Omega^{-1}\text{m}^{-2}$, which is close to the G_s obtained in our experiments. This highlights the importance of spin-relaxation induced by the thermal motion of the YIG magnetization, as discussed in the main text. Geometrical enhancement of the modulation can be obtained by reducing t_{Al}, as shown in Fig. S5(d), thereby maximizing spin-absorption at the Al/YIG interface [16].

II. Three dimensional (3D) spin transport model

Here we describe the our 3D spin transport model used to analyze our data. It is similar to that described in Ref. 20 for collinear spin transport with the possibility of studying spin-relaxation effects (i) due to the spin-mixing conductance at the Al/YIG interface as well as (ii) Hanle spin-precession due to the in-plane magnetic field [see Sec. III below for detail]. The charge current $j_c^\alpha(\vec{r})$ and spin current $\boldsymbol{j}_s^\alpha(\vec{r})$, for $j_c^\alpha(\vec{r})$ (where $\alpha \in x,y,z$), are related to the charge $\mu_c(\vec{r})$ and spin potentials $\boldsymbol{\mu}_s$ as

$$\begin{pmatrix} j_c^\alpha(\vec{r}) \\ \boldsymbol{j}_s^\alpha(\vec{r}) \end{pmatrix} = -\begin{pmatrix} \sigma & \alpha_F\sigma \\ \alpha_F\sigma & \sigma \end{pmatrix}\begin{pmatrix} \vec{\nabla}\mu_c \\ \vec{\nabla}\boldsymbol{\mu}_s \end{pmatrix} \tag{9}$$

where σ is the bulk conductivity and α_F is the bulk spin polarization of the conductivity. The device geometry we model is shown in Fig. S5(a), showing schematic source-drain configurations as well as voltage contacts. We impose charge flux at contact 1 and drain it at 2. The nonlocal voltage, due to spin diffusion, is obtained by taking the difference between the surface integrated μ_c at contacts 3 and 4 , both for the parallel (P) or antiparallel (AP) magnetization configurations. To solve Eq. (9), we use conservation laws for charge ($\nabla\cdot j_c^\alpha(\vec{r}) = 0$) and spin current ($\nabla\cdot\boldsymbol{j}_s = (1-\alpha_F^2)\sigma\boldsymbol{\mu}_s/\lambda^2$) with spin precession due to the in-plane applied field also included in the model. By defining an angle α between $\boldsymbol{\mu}_s$ and the YIG magnetization $\hat{m}$ and allowing for a boundary spin current at the Al/YIG interface using Eq. 1 of the main text, we can study the transport of spins in NLSV devices and their interaction with the YIG magnetization. The material parameters for the model, σ, α_F and λ_s are taken from Ref. [23]. Our modeling procedure involves, first, fitting of the measured NLSV signal on a SiO_2 substrate by varying α_F and using $\lambda_N = 350$nm. Next, we aim to find G_s of the Al/YIG interface that properly quantifies spin transport properties of the YIG sample. Figure S5(b) shows the dependence of the NLSV signal on G_s. As expected, when G_s very low, the NLSV signal is not affected by the presence of the YIG as spins are not lost to the substrate. For $G_s \simeq 5\times10^{13}\Omega^{-1}\text{m}^{-2}$ we obtain the experimentally measured NLSV signal (shown in red dashed line). For even larger G_s values, the effect is maximum with the NLSV signal falling by almost one order of magnitude. It is important to remember that the value of G_s that is extracted here is a simple measure of spin-flip processes at the Al/YIG interface due to thermal fluctuation of the YIG magnetization or disorder induced effects. At the temperatures of our experiment it is difficult to distinguish which one of the two processes is dominant.

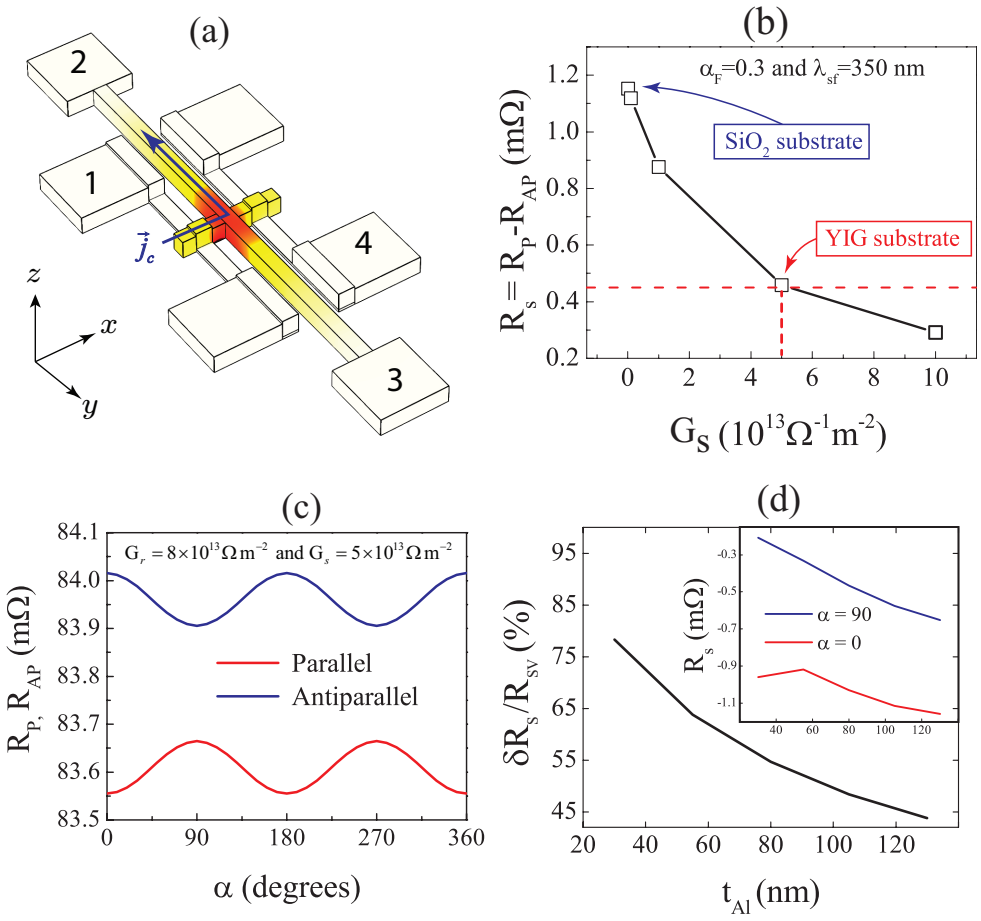

FIG. 5. (a) Geometry of the modeled device showing the measurement configuration with a 3D profile and the y-component of the spin accumulation. (b) The dependence of the NLSV signal on the effective (collinear) spin mixing conductance G_s. To reproduce the experimentally observed decrease in the spin signal from SiO_2 to the YIG substrate, an effective spin mixing conductance of $G_s = 5 \times 10^{13}\ \Omega^{-1}\mathrm{m}^{-2}$ is required. (c) The dependence of the NLSV signal on the angle between $\hat{m}$ and $\boldsymbol{\mu}_s$ for $G_s = 5 \times 10^{13}\ \Omega^{-1}\mathrm{m}^{-2}$. (d) The dependence of the spin signal modulation amplitude on the thickness of the Al channel signifying the interplay between the spin-mixing conductance and the spin-conductance in the Al channel.

For the angular dependent simulation we only vary the angle α between $\boldsymbol{\mu}_s$ and $\hat{m}$ while keeping all other parameters constant (such as α_F, λ_N $G_s = 5 \times 10^{13}\ \Omega^{-1}\mathrm{m}^{-1}$ and $G_r = 8 \times 10^{13}\ \Omega^{-1}\mathrm{m}^{-1}$). As shown in Fig. S5(b) our simulation as described above reproduces the $\cos^2(\alpha)$ dependence observed in our experiments as well as by Villamor *et al.* [16].

For the extracted values of G_r from our analysis, the experimentally observed modulation of the NLSV signal by the rotating magnetization direction of the YIG is small. Possible ways to enhance the modulation are to 1) maximize the spin-mixing conductance via controlled interface engineering of the Al/YIG interface or 2) reduce the thickness of the spin transport channel. In the latter, for a fixed G_r, the effect of decreasing the thickness of the spin transport channel is to effectively reduce the spin conductance G_N along the channel thereby maximizing the spin current through the Al/YIG interface. Figure S5(c) shows the thickness dependence of the modulation of the spin signal $\delta R_s = R_s(\alpha = 0^0) - R_s(\alpha = 90^0)$ normalized by R_s as a function of the thickness t_{Al}, with the inset showing that for the P and AP configurations. As the thickness of the Al channel increases the spin current absorption at the Al/YIG interface decreases or vice versa.

III. Investigation of possible alternative explanations for the observed modulation

It can be argued that the experimentally observed modulation of the NLSV signal can be fully explained by (i) the Hanle spin-precession and/or (ii) the rotation of the magnetizations of the injector/detector electrodes due to the 5 mT in-plane magnetic field. Below, we show that even the combined effect of both mechanisms is too small to explain the experimentally observed modulation of the NLSV signal.

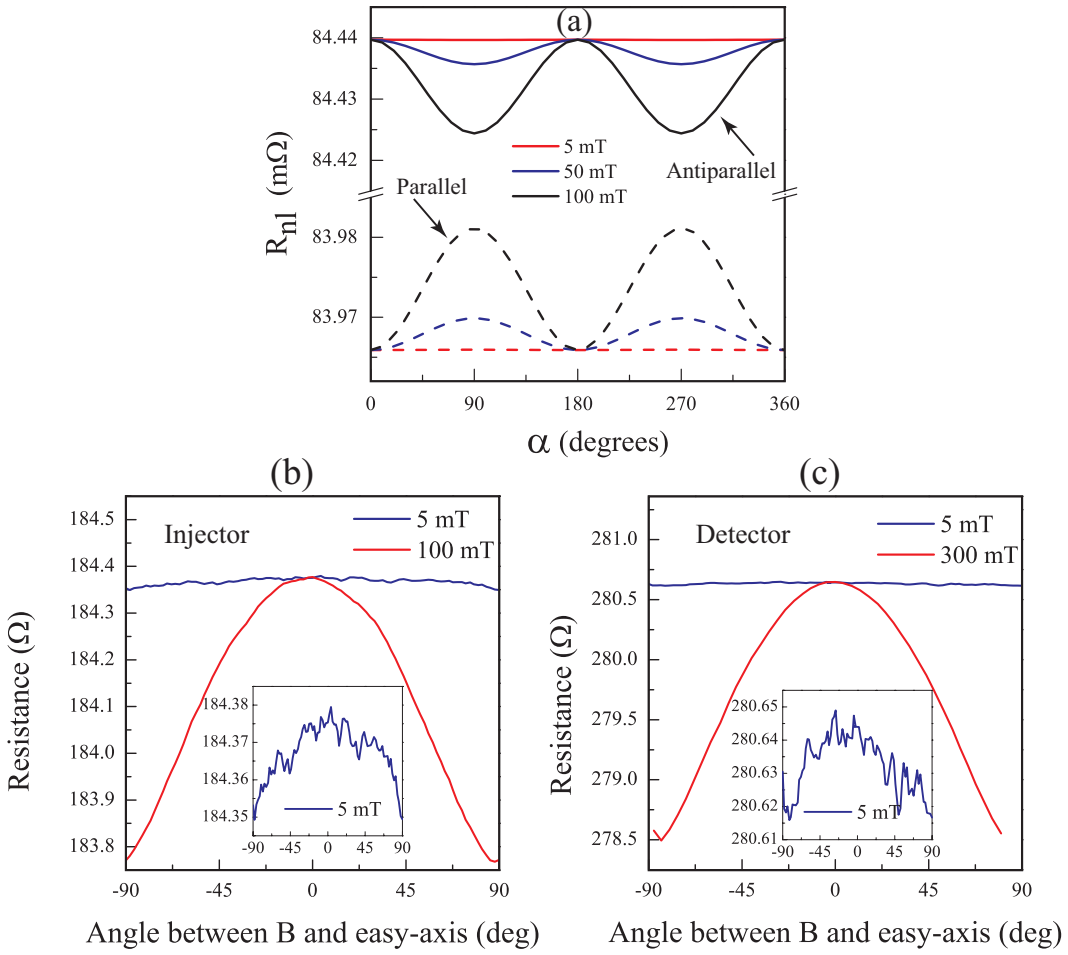

FIG. 6. (a) Modulation of the NLSV when only considering the Hanle effect due to the in-plane magnetic field in the P (dashed lines) and AP (solid lines) at 5 mT (red), 50 mT (blue) and 100 mT (black). see text for more details. (b) Anisotropic magnetoresistance (AMR) measurement for the injector (left) and detector (right) ferromagnets at two different magnetic fields. The insets show the full-scale plot of the measurements at 5mT.

A. Hanle spin-precession induced modulation of the NLSV signal

Spins precessing around an in-plane magnetic field $\vec{B}$ would acquire an average spin precession angle of $\phi = \omega_L \tau_D$, where $\omega_L = g\mu_B \vec{B}/\hbar$ is the Larmor precession frequency, $\tau_D = L^2/2D_c = 25$ ps is the average diffusion time an electron takes to traverse the distance L between the injector and the detector and $D_c = 0.005\text{m}^2/\text{s}$ is the diffusion coefficient [26]. For an applied field of 5 mT and L=500 nm, we obtain $\phi = 1.25^o$, giving us a maximum contribution of $1 - \cos\phi$ =~0.02% [see Eq. (10)] to the experimentally observed signal (compared to the ~12% in Fig. 3(b) of the main text). This is expected because the spin-precession frequency ω_L^{-1} (~8 ns) at such magnetic fields is three orders of magnitude slower than τ_D.

This simple estimate is further supported by our 3D finite element model as we show next. Figure S6(a) shows the angle dependence of the nonlocal signal due to an in-plane magnetic field when we only consider the Hanle effect both for the AP (solid lines) and P (dashed lines) configurations at three different magnetic field values of 5 mT (red), 50 mT (blue) and 100 mT (black). The maximum modulation of the NLSV signal that the Hanle effect presents is only 0.001% at the measurement field of 5 mT and only become relevant at high fields. Therefore, the Hanle effect alone can not explain the results presented in the main text.

B. Magnetization rotation induced modulation of the NLSV signal

The in-plane rotation of the sample under an applied magnetic field of 5 mT might induce rotations in the magentization of the injector/detector electrodes. In such a case, a relative angle θ_r between the magnetization direction of the injector and detector electrodes would result in a modulation of the NLSV signal given by

$$\frac{\delta R_{\text{nl}}}{R_{\text{nl}}(\theta_r = 0)} = \frac{R_{\text{nl}}(\theta_r = 0) - R_{\text{nl}}(\theta_r)}{R_{\text{nl}}(\theta_r = 0)} = \pm|1 - \cos\theta_r|, \tag{10}$$

with +(−) corresponding to the P (AP) configuration. Using Eq. (10), we find that a relative angle $\theta_r \simeq 28^o$ between the magnetization directions of the injector and detector is required in order to explain the experimentally observed modulation. To determine the field induced in-plane rotation of the magnetization by the applied magnetic field, we carried out angle dependent anisotropic magnetoresistance (AMR) measurements both for the injector and detector electrodes, using a new set of devices with identical dimensions. The AMR measurements were repeated for different magnetic field strengths, at 5 mT and at higher magnetic fields of 100 mT and 300 mT.

Figure S6(b) and (c) show the two-probe AMR measurement of the injector and detector electrodes, respectively, at two different magnetic fields. For the injector electrode in Fig. S6(b), at an applied field of 100 mT (red line), an AMR response $\Delta R = R_{\parallel} - R_{\perp} = 0.6\ \Omega$ is observed, where $R_{\parallel}(R_{\perp})$ is the resistance of the ferromagnet when the angle between the applied field and the easy axis is $\theta = 0^o$ ($\theta = 90^o$). For the same electrode, at an applied field of 5 mT (blue line, see also the inset), the AMR response is only 0.025 Ω. Now, by comparing these two measurements we conclude that the effect of the 5 mT field would be to rotate the magnetization of this electrode by a maximum angle $\theta_1 = 15^o$ from the easy axis. A similar analysis for the detector electrode, using the AMR responses of 2 Ω (at 300 mT) and 0.025 Ω (at 5 mT) in Fig. S6(c), yields a maximum magnetization rotation $\theta_2 = 10^o$. Relevant here is the net relative magnetization rotation between the two electrodes $\theta_r = \theta_1 - \theta_2 = 5^o$ and, using Eq. (10), we conclude that it would only cause a modulation of 0.4 %, which is much smaller than the 12% observed in our experiments. Our analysis based on the AMR effect is equivalent to that in Ref. 16 where magneto-optical Kerr effect measurements were used to exclude a possible in-plane magnetization rotation as the origin for the observed modulation in the nonlocal spin valve signal [16].

To summarize this section, the Hanle effect and the magnetization rotation induced by the in-plane magnetic field neither separately nor when combined are sufficient to explain the experimentally observed modulation. Only after including the effect of the spin-mixing interaction via $G_{\uparrow\downarrow}$ that it is possible to reproduce the modulation observed in the experiments.

* e-mail:f.k.dejene@gmail.com

[1] K. Uchida, J. Xiao, H. Adachi, J. Ohe, S. Takahashi, J. Ieda, T. Ota, Y. Kajiwara, H. Umezawa, H. Kawai, *et al.*, Nature materials **9**, 894 (2010).

[2] V. Castel, N. Vlietstra, J. Ben Youssef, and B. J. van Wees, Applied Physics Letters **101**, 132414 (2012).

[3] M. Althammer, S. Meyer, H. Nakayama, M. Schreier, S. Altmannshofer, M. Weiler, H. Huebl, S. Geprägs, M. Opel, R. Gross, D. Meier, C. Klewe, T. Kuschel, J.-M. Schmalhorst, G. Reiss, L. Shen, A. Gupta, Y.-T. Chen, G. Bauer, E. Saitoh, and S. Goennenwein, Phys. Rev. B **87**, 224401 (2013).

[4] N. Vlietstra, J. Shan, V. Castel, B. J. van Wees, and J. Ben Youssef, Physical Review B **87**, 184421 (2013).

[5] J. Flipse, F. K. Dejene, D. Wagenaar, G. E. W. Bauer, J. B. Youssef, and B. J. van Wees, Phys. Rev. Lett. **113**, 027601 (2014).

[6] J. Xiao, G. E. W. Bauer, K.-c. Uchida, E. Saitoh, and S. Maekawa, Physical Review B **81**, 214418 (2010).

[7] X. Jia, K. Liu, K. Xia, and G. E. W. Bauer, EPL (Europhysics Letters) **96**, 17005 (2011).

[8] B. Heinrich, C. Burrowes, E. Montoya, B. Kardasz, E. Girt, Y.-Y. Song, Y. Sun, and M. Wu, Physical Review Letters **107**, 066604 (2011).

[9] Y.-T. Chen, S. Takahashi, H. Nakayama, M. Althammer, S. T. B. Goennenwein, E. Saitoh, and G. E. W. Bauer, Physical Review B **87**, 144411 (2013).

[10] M. Weiler, M. Althammer, M. Schreier, J. Lotze, M. Pernpeintner, S. Meyer, H. Huebl, R. Gross, A. Kamra, J. Xiao, Y.-T. Chen, H. Jiao, G. Bauer, and S. Goennenwein, Phys. Rev. Lett. **111**, 176601 (2013).

[11] S. Huang, X. Fan, D. Qu, Y. Chen, W. Wang, J. Wu, T. Chen, J. Xiao, and C. Chien, Phys. Rev. Lett. **109**, 107204 (2012).

[12] T. Kikkawa, K. Uchida, S. Daimon, Y. Shiomi, H. Adachi, Z. Qiu, D. Hou, X.-F. Jin, S. Maekawa, and E. Saitoh, Physical Review B **88**, 214403 (2013).

[13] F. J. Jedema, M. V. Costache, H. B. Heersche, J. J. A. Baselmans, and B. J. van Wees, Applied Physics Letters **81** (2002).

[14] F. J. Jedema, M. S. Nijboer, A. T. Flip, and B. J. van Wees, Physical Review B **67**, 085319 (2003).

[15] T. Kimura, T. Sato, and Y. Otani, Physical Review Letters **100**, 066602 (2008).

[16] E. Villamor, M. Isasa, S. Vélez, A. Bedoya-Pinto, P. Vavassori, L. E. Hueso, F. S. Bergeret, and F. Casanova, Phys. Rev. B **91**, 020403 (2015).

[17] V. Castel, N. Vlietstra, B. J. van Wees, and J. B. Youssef, Physical Review B **86**, 134419 (2012).

[18] Z. Qiu, K. Ando, K. Uchida, Y. Kajiwara, R. Takahashi, H. Nakayama, T. An, Y. Fujikawa, and E. Saitoh, Applied Physics Letters **103**, 092404 (2013).

[19] See supplemental material for the derivation of Eq. 3, detailed procedure of the finite element simulation and additional control experiments.

[20] A. Slachter, F. L. Bakker, and B. J. van Wees, Phys. Rev. B **84**, 174408 (2011).

[21] V. S. Rychkov, S. Borlenghi, H. Jaffres, A. Fert, and X. Waintal, Phys. Rev. Lett. **103**, 066602 (2009).

[22] F. L. Bakker, A. Slachter, J.-P. Adam, and B. J. van Wees, Phys. Rev. Lett. **105**, 136601 (2010).

[23] F. K. Dejene, J. Flipse, G. E. W. Bauer, and B. J. van Wees, Nature Physics **9**, 636 (2013).

[24] M. Schreier, A. Kamra, M. Weiler, J. Xiao, G. E. W. Bauer, R. Gross, and S. T. B. Goennenwein, Physical Review B **88**, 094410 (2013).

[25] T. Valet and A. Fert, Physical Review B **48**, 7099 (1993).

[26] F. J. Jedema, M. V. Costache, H. B. Heersche, J. J. A. Baselmans, and B. J. van Wees, Applied Physics Letters **81** (2002).